Title

A probability density function model describing height estimation uncertainty due to image pixel intensity noise in digital fringe projection measurements

Authors

O'Dowd, Niall M
Wachtor, Adam J
Todd, Michael D

Publication Date

2021-03-01

DOI

10.1016/j.optlaseng.2020.106422

Peer reviewed

A PROBABILITY DENSITY FUNCTION MODEL DESCRIBING HEIGHT ESTIMATION UNCERTAINTY DUE TO IMAGE PIXEL INTENSITY NOISE IN DIGITAL FRINGE PROJECTION MEASUREMENTS

Niall M. O'Dowd[1], Adam J. Wachtor[2], and Michael D. Todd[3]

[1,3]Department of Structural Engineering, University of California San Diego
[2]Engineering Institute, Los Alamos National Laboratory
[1]nmodowd@eng.ucsd.edu, [2]ajw@lanl.gov, [3]mdtodd@eng.ucsd.edu (corresponding author)

Key words: Digital Fringe Projection; Height Estimation; Uncertainty Quantification; Pixel Intensity Noise

Abstract. Digital fringe projection is a surface-profiling technique used for highly accurate non-contact measurements. As with any measurement technique, a variety of sources degrade to the measurement accuracy of the method. This paper presents an analytically-derived probability density function that explicitly models the surface height measurement error due to inevitable phase measurement error, and it includes the specific case of pixel noise inducing the phase measurement error that ultimately leads to the height estimation error. The accuracy of the model was validated through Monte-Carlo simulations of resultant height distributions subject to arbitrarily correlated pixel intensity noise and experimental digital fringe projection measurements where the pixel-by-pixel height uncertainty estimations were compared to the predictions of the derived model.

1 Introduction

Digital fringe projection (DFP) is a non-contact surface measurement technique used in surface height profiling, surface roughness quantification, and three-dimensional point cloud creation, among other areas. As commercial availability of high accuracy projectors and digital cameras increases, this versatile measurement technique has become even more popular for highly critical engineering applications drawn from biomedical [1–3], materials science [4–6], and electronics inspection [7, 8] domains. When such measurements are used to inform decisions regarding part acceptance, maintenance, or usage, it is important to understand and quantify uncertainties in the measurement process prior to implementation. Potential sources for measurement uncertainty in the DFP method include projector gamma nonlinearity [9–11], projector and camera quantization effects [12–14], and pixel intensity noise [15–18]. Substantial work has been made to quantify and mitigate the height profile measurement error caused by non-linear projector gamma [19–22] and other publications address measurement uncertainty and mitigation caused by projector and camera quantization [23–25].

Pixel intensity noise is one of the major sources of error in DFP height profilometry [26], and has been mentioned for decades in classical works on the DFP method [27, 28]. It has motivated development of new phase-shifting algorithms [17, 18], and has been reported to dominate the error contributions from camera and projection quantization error [29]. Even with the development of nonlinear gamma error reduction, measurement uncertainty contributions from noise in the pixel field is unavoidable [15]. However, to the authors' knowledge, no work has been published which explicitly provides a forward analytical model of the measurement height uncertainty caused by phase noise. In

this work, a probability density function (PDF) model is developed that expresses how phase noise error propagates into resultant height measurement uncertainty. The specific case where pixel intensity noise is the source of the phase measurement noise is then outlined, ultimately providing an expression that relates pixel noise to height measurement uncertainty in the DFP measurement process.

Other works have considered height estimation uncertainty due to phase noise in previous alternative ways. The work of G. Notni et al. [29] summarized a variety of phase errors due to the digital camera and projector in DFP phase measurement, but it did not include height-converted phase noise analysis nor an analytically derived model for the phase measurement dispersion caused by the quantization errors. Creath [30] proposed a specialized technique utilizing two-wavelength phase shifting, and reported the height noise impact of the approach, but it did not provide a quantitative measure of the phase or pixel noise contributions to height measurement. Two studies by An et al. [31, 32] proposed and evaluated a method which uses geometric constraints for phase-unwrapping, specifically used in low low signal-to-noise ratio phase measurement. These works also did not provide a rigorous method for modeling resultant height uncertainty. Tang et. al [33] developed a method of analysis to obtain height incorporating demodulation and convolution techniques. In their study, phase error was reduced using signal processing techniques, quantified, and converted to height error, but did not include a formal estimation of the propagation of intensity or phase noise into height measurement. A common theme among most published works thus far is an abundance of techniques which alleviate phase (and ultimately height) error, benchmarked on known measured objects, but the contributions of alleviated error sources are usually not modeled from a fundamental level. The work presented in this study advances DFP metrology by providing such a method for statistically modeling height measurement uncertainty from contributions of phase error. We then continue the derivation to include the specific and important case of pixel noise sources converting to phase error (described in detail in O'Dowd et al. [34]) and how that propagates to height estimation uncertainty. The height uncertainty model is compared against Monte-Carlo MC simulation as well as an ensemble of surface measurements with a prototype DFP measurement system, demonstrating the model's efficacy. Ultimately, this model can be used to estimate order statistics–and thus quantify–the height uncertainty in the DFP measurement process using measured noise properties from the pixel field.

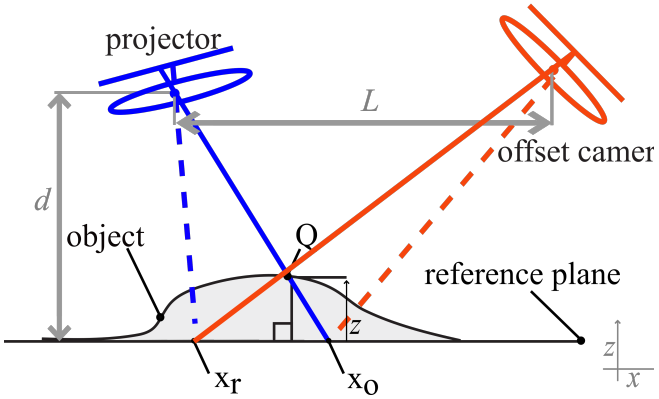

Figure 1: A general two-dimensional schematic of the digital fringe projection measurement.

Commonly, DFP height measurements are made by projecting patterns onto a flat reference plane (physical or mathematical, denoted further with subscript "r"), then placing an object onto the scene, and recording how the projected patterns deform from the object's shape (denoted further with "o"). A

representative DFP experimental setup schematic is shown in Figure 1. The projected patterns are often sinusoidally varying computer generated images, known as "fringes", with pixel value f assigned according to

$$f_i(x) = R(\cos(\frac{2\pi x}{P} + \delta_i) + 1), \tag{1}$$

where R is a scaling factor related to fringe brightness, P is the fringe pitch, and N phase-shifted images are generated and projected onto both reference and object with (equipartitioned) spatial shifts of $\delta_i = 2\pi i/N$, $i = 1...N$ (further referred to as "projections," where i is the projection index). Equation 1 creates a fringe pattern with varying intensity as a function of x, as it relates to Figure 1.

The camera records images of the incident fringes on both reference and object surfaces, where the intensity $I_{(r,o)}$ of any fringe incident on a surface (either the reference r or object o) at any given measurement point $x_{r,o}$ is given by [35] as

$$I_{(r,o)} = A_{(r,o)} + B_{(r,o)} \cos\left(2\pi x_{(r,o)}/P\right), \tag{2}$$

where $\phi_{(r,o)} = 2\pi x_{(r,o)}/P$ is the phase, and $A_{(r,o)}$ and $B_{(r,o)}$ are the background intensity due to projector bias (combined with ambient light intensity) and the projected fringe contrast, respectively, at the arbitrary point $x_{(r,o)}$. In order to recover differential information between object and reference phases, which is functionally related to the object height [36], the measurement point's "i-th" projection intensity in Equation 2 may be each written as

$$I_{(r,o),i} = A_{(r,o),i} + B_{(r,o),i} \cos\left(\phi_{(r,o)} + \delta_i + \phi_c\right), \tag{3}$$

where ϕ_c accounts for the phase offset of the point in relation to the carrier phase (undeformed phase of the projected fringe pattern), and subscript "i" is the projection index. Once images are recorded of the projected fringes on the reference and object, phase $\phi_{r,o}$ (either on the reference or object), is found by

$$\phi_{(r,o)} = \arctan\left(\frac{-\sum_{i=1}^{N} I_{(r,o),i} \sin\delta_i}{\sum_{i=1}^{N} I_{(r,o),i} \cos\delta_i}\right), \tag{4}$$

where it is assumed that nonlinear projector gamma issues are negligible or appropriately corrected/calibrated. The differential phase measurement ϕ between object and reference that ultimately is used to determine the measurement point's height above the reference surface is given by

$$\begin{aligned} \phi &= \phi_o - \phi_r \\ &= \arctan\left(\frac{-\sum_{i=1}^{N} I_{o,i} \sin\delta_i}{\sum_{i=1}^{N} I_{o,i} \cos\delta_i}\right) - \arctan\left(\frac{-\sum_{i=1}^{N} I_{r,i} \sin\delta_i}{\sum_{i=1}^{N} I_{r,i} \cos\delta_i}\right) \qquad (5) \\ &= \frac{2\pi\left(x_o - x_r\right)}{P}. \qquad (6) \end{aligned}$$

Geometrically, the height of a measurement point z from a reference point can be represented as a function of the geometries of the DFP experimental setup and the scalar quantities x_r and x_o, seen in Figure 1. This relationship can be written as

$$z = \frac{d\left(x_o - x_r\right)}{L + x_o - x_r}, \tag{7}$$

where d and L are the distance between the projector and the reference plane, and the distance between the projector and the camera, respectively. Combining Equations 6 and 7, we can express z as a function of the measured differential phase ϕ and geometrical properties of the DFP system as

$$z(\phi) = \frac{P\phi d}{2\pi L + P\phi}. \tag{8}$$

Many applications of the DFP method use a linearized phase-to-height measurement model, which assumes that the spacing between the projector and camera components is much larger than the geometric distance between reference and object ray projections x_r and x_o, i.e. $L >> (x_o - x_r)$. Effectively, this assumption is valid for small height measurements. This assumption simplifies the principal height measurement relationship to a linearized version, z_l, given by

$$\begin{aligned} z_l &= \frac{d\,(x_o - x_r)}{L} \\ &= \frac{Pd\phi}{2\pi L}. \end{aligned} \tag{9}$$

Comparing Equation 9 to Equation 8, we see that indeed the linearized version expresses a proportional relationship between estimated height z_l and differential phase measurement ϕ.

2 Output Height Uncertainty Model

2.1 Fully Nonlinear Height Model

The measured differential phase ϕ inherently contains noise, κ, which arises from a variety of sources, and this noise will propagate through the phase-to-height transformation yielding uncertainty in the estimated height measurement. We may then define the height measurement residual error χ by adding this noise κ to the differential phase measurement ϕ and subtracting the true height value, $\chi = z(\phi + \kappa) - z(\phi)$. The noisy differential phase $\phi + \kappa$ is then substituted from Equation 8, yielding

$$\begin{aligned} \chi &= z(\phi + \kappa) - z(\phi) \\ &= \frac{P(\phi + \kappa)d}{2\pi L + P(\phi + \kappa)} - \frac{P\phi d}{2\pi L + P\phi} \\ &= \frac{\kappa P(d - z)^2}{2\pi L d + \kappa P(d - z)}, \end{aligned} \tag{10}$$

where we substitute in for ϕ from the inverse of Equation 8 to arrive at the form relating height uncertainty χ as a function of phase noise κ, true height z, and DFP measurement system parameters d, P, L.

Assuming the probability density function of the phase noise, $p\,(\kappa)$, is known or can otherwise be modeled, we may use the change of variables technique to find the probability density function associated with the single point height measurement uncertainty, $p\,(\chi)$, as

$$p(\chi) = \frac{p(\kappa)}{|\partial\chi/\partial\kappa|}$$

$$
\begin{aligned}
&= \frac{p(\kappa)(2\pi Ld + \kappa P(d-z))^2}{2\pi LP(d-z)^2 d} \\
&= \frac{2\pi Ldp(\kappa)}{P(\chi+z-d)^2} \\
&= \frac{2\pi Ldp\left(\frac{2\pi Ld\chi}{P(d-z)(d-z-\chi)}\right)}{P(\chi+z-d)^2},
\end{aligned} \tag{11}
$$

where in the final form we have substituted in for κ from the inverse of Equation 10.

Equation 11 is a very general form for any phase noise PDF model form, $p(*)$. In previous work, we derived a PDF for phase noise arising from pixel intensity noise, given in Equations 21-22 of [34]. Combining that previously-derived PDF with Equations 11 and substituting for κ using the inverse of Equation 10 yields

$$
p(\chi) = \frac{e^{-z_3}\sec^2\frac{2\pi L\chi d}{P(d-z)(d-\chi-z)}\left(1+\sqrt{\pi}z_2 e^{z_2^2}\left(\mathrm{erf}\left(z_2\right)\pm 1\right)\right)Ld}{P(-d+\chi+z)^2 z_1\sqrt{1-\rho_{XY}^2}}, \tag{12}
$$

where

$$
\begin{aligned}
z_1 &= \frac{\sigma_Y^2 - 2\rho_{XY}\sigma_X\sigma_Y\tan\frac{2\pi L\chi d}{P(d-z)(d-\chi-z)} + \sigma_X^2\tan^2\frac{2\pi L\chi d}{P(d-z)(d-\chi-z)}}{\sigma_X\sigma_Y\left(1-\rho_{XY}^2\right)}, \\
z_2 &= \frac{\mu_Y\sigma_X\left(\rho_{XY}\sigma_Y - \sigma_X\tan\frac{2\pi L\chi d}{P(d-z)(d-\chi-z)}\right) + \mu_X\sigma_Y\left(\sigma_X\rho_{XY}\tan\frac{2\pi L\chi d}{P(d-z)(d-\chi-z)} - \sigma_Y\right)}{\sqrt{2}\sigma_X\sigma_Y\sqrt{1-\rho_{XY}^2}\sqrt{\sigma_Y^2 - 2\rho_{XY}\sigma_X\sigma_Y\tan\frac{2\pi L\chi d}{P(d-z)(d-\chi-z)} + \sigma_X^2\tan^2\frac{2\pi L\chi d}{P(d-z)(d-\chi-z)}}}, \\
z_3 &= \frac{\mu_Y^2\sigma_X^2 + \mu_X^2\sigma_Y^2 - 2\mu_X\mu_Y\sigma_X\sigma_Y\rho_{XY}}{2\sigma_X^2\sigma_Y^2\left(1-\rho_{XY}^2\right)},
\end{aligned} \tag{13}
$$

and where $\mathrm{erf}(*)$ is the standard error function. Quantities σ_Y, σ_X, and ρ_{XY} are functions of measured pixel intensity noise shown in [34]. These quantities are intrinsically related to the standard deviation and correlation of random variables functionally related to ensembles of measured image intensities from experiment. Correlation in the noise structure may arise from periodic lighting fluctuations such as overhead fluorescent lights, projector gamma error, or dust particle patterns on either optics lens. In Section 3.2, we show an example of object and reference noise correlation, which contributes to the formulation of quantities σ_Y, σ_X, and ρ_{XY}. Also shown in detail in our previous work, the evaluation of $p(\kappa)$ required separation into two integration regions, where the minus sign $(-)$ is used when $|\kappa| < \pi/2$, and the plus sign $(+)$ is used when $\pi > |\kappa| > \pi/2$. The change of variables technique requires updating these conditions using Equation 12, requiring the minus sign $(-)$ when $|\chi| < \frac{\pi P(d-z)^2}{2\left(2\pi Ld+\frac{1}{2}\pi P(d-z)\right)}$, and taking the plus sign $(+)$ when $\frac{\pi P(d-z)^2}{\left(2\pi Ld+\frac{1}{2}\pi P(d-z)\right)} > |\chi| > \frac{\pi P(d-z)^2}{2\left(2\pi Ld+\frac{1}{2}\pi P(d-z)\right)}$.

Equation 12 completely determines the single-point probability density function of height measurement uncertainty for any arbitrarily-correlated Gaussian pixel intensity noise. A special case occurs when the pixel intensity noise structure has no inter-projection correlations, no correlations between reference object and test object data, and the noise standard deviations in each object and each reference image are the same for all projections and zero-mean; in [34] Equation 24 we showed the reduced form of $p(\kappa)$ for this case. Combining this form with Equation 11 results in a height

uncertainty distribution

$$p(\chi) = \frac{e^{\frac{-N}{4(\sigma_o^2+\sigma_r^2)}} Ld}{P(-d+\chi+z)^2} \left(\frac{e^{\frac{N\cos^2\frac{2\pi L\chi d}{P(d-z)(d-\chi-z)}}{4(\sigma_o^2+\sigma_r^2)}} \sqrt{\pi}\sqrt{N\cos^2\frac{2\pi L\chi d}{P(d-z)(d-\chi-z)}} \left(\operatorname{erf}\left(\frac{1}{2}\sqrt{\frac{N\cos^2\frac{2\pi L\chi d}{P(d-z)(d-\chi-z)}}{\sigma_o^2+\sigma_r^2}} \right) \pm 1 \right)}{2\sqrt{\sigma_o^2+\sigma_r^2}} + 1 \right), \quad (14)$$

where σ_r and σ_o are the noise standard deviations in the reference and object images scaled by fringe contrast, respectively.

2.2 Linearized Height Uncertainty Model

Proceeding exactly as with the derivation in Section 2.1, we can derive a height uncertainty model for the linearized height measurement case as well. We define the linearized residual height measurement noise as $\chi_l = z_l(\phi+\kappa) - z_l(\phi)$, and combining with Equation 9 provides

$$\chi_l = \frac{P(\phi+\kappa)d}{2\pi L} - \frac{P\phi d}{2\pi L} = \frac{\kappa P d}{2\pi L}. \quad (15)$$

The change of variables technique gives the height uncertainty distribution as

$$\begin{aligned} p(\chi_l) &= \frac{p(\kappa)}{|\partial\chi_l/\partial\kappa|} \\ &= \frac{2\pi L p(\kappa)}{Pd} \\ &= \frac{2\pi L p\left(\frac{2\pi L\chi_l}{Pd}\right)}{Pd}. \end{aligned} \quad (16)$$

For the same specific phase noise model described in the previous subsection, we may similarly combine Equation 16 with the PDF derived in [34] and substitute for κ using the inverse of Equation 15 to get

$$p(\chi_l) = \frac{e^{-z_3}\sec^2\frac{2\pi L\chi_l}{Pd}\left(1+\sqrt{\pi}z_2 e^{z_2^2}\left(\operatorname{erf}(z_2)\pm 1\right)\right)L}{z_1\sqrt{1-\rho_{XY}^2}Pd}, \quad (17)$$

where

$$\begin{aligned} z_1 &= \frac{\sigma_Y^2 - 2\rho_{XY}\sigma_X\sigma_Y\tan\frac{2\pi L\chi_l}{Pd} + \sigma_X^2\tan^2\frac{2\pi L\chi_l}{Pd}}{\sigma_X\sigma_Y\left(1-\rho_{XY}^2\right)}, \\ z_2 &= \frac{\mu_Y\sigma_X\left(\rho_{XY}\sigma_Y - \sigma_X\tan\frac{2\pi L\chi_l}{Pd}\right) + \mu_X\sigma_Y\left(\sigma_X\rho_{XY}\tan\frac{2\pi L\chi_l}{Pd} - \sigma_Y\right)}{\sqrt{2}\sigma_X\sigma_Y\sqrt{1-\rho_{XY}^2}\sqrt{\sigma_Y^2 - 2\rho_{XY}\sigma_X\sigma_Y\tan\frac{2\pi L\chi_l}{Pd} + \sigma_X^2\tan^2\frac{2\pi L\chi_l}{Pd}}}, \\ z_3 &= \frac{\mu_Y^2\sigma_X^2 + \mu_X^2\sigma_Y^2 - 2\mu_X\mu_Y\sigma_X\sigma_Y\rho_{XY}}{2\sigma_X^2\sigma_Y^2\left(1-\rho_{XY}^2\right)}, \end{aligned} \quad (18)$$

and the quantities σ_Y, σ_X, and ρ_{XY} are, as before. Similar to the fully nonlinear version in Section 2.1, the derivation requires updating the conditions of the previously-derived $p(\kappa)$ distribution, using

Equation 15. This results in using the minus sign $(-)$ in Equation 17 when $|\chi_l| < \frac{Pd}{4L}$, and the plus sign $(+)$ when $\frac{Pd}{2L} > |\chi_l| > \frac{Pd}{4L}$. Equation 17 is the linearized height measurement model analogue to Equation 12.

Finally, for the special case of pixel intensity noise structure described above, the linearized model analogous to Equation 14 is

$$p(\chi_l) = \frac{e^{\frac{-N}{4(\sigma_o^2+\sigma_r^2)}}L}{Pd}\left(\frac{e^{\frac{N\cos^2\frac{2\pi L\chi_l}{Pd}}{4(\sigma_o^2+\sigma_r^2)}}\sqrt{\pi}\sqrt{N\cos^2\frac{2\pi L\chi_l}{Pd}}\left(\operatorname{erf}\left(\frac{1}{2}\sqrt{\frac{N\cos^2\frac{2\pi L\chi_l}{Pd}}{\sigma_o^2+\sigma_r^2}}\right)\pm 1\right)}{2\sqrt{\sigma_o^2+\sigma_r^2}}+1\right). \quad (19)$$

3 Model Verification

3.1 Monte-Carlo Simulation

Ensembles of MC simulated phase measurements ϕ_{MC} were created in order to verify the derived height uncertainty models from Section 2, with varying levels of pixel noise correlation and standard deviation, each using 98304 samples. We created the MC ensembles by adding pixel intensity noise $\epsilon_{r,o}$ to the $I_{r,o}$ terms in Equation 5 and combining Equations 8 and 9 for the full MC model and the linear MC model, respectively, giving

$$z_{MC} = \frac{Pd\left(\arctan\left(\frac{-\sum_{i=1}^{N}(I_{o,i}+\bar{\epsilon}_{o,i})\sin\delta_i}{\sum_{i=1}^{N}(I_{o,i}+\bar{\epsilon}_{o,i})\cos\delta_i}\right)-\arctan\left(\frac{-\sum_{i=1}^{N}(I_{r,i}+\bar{\epsilon}_{r,i})\sin\delta_i}{\sum_{i=1}^{N}(I_{r,i}+\bar{\epsilon}_{r,i})\cos\delta_i}\right)\right)}{2\pi L+P\left(\arctan\left(\frac{-\sum_{k=1}^{N}(I_{o,i}+\bar{\epsilon}_{o,i})\sin\delta_i}{\sum_{i=1}^{N}(I_{o,i}+\bar{\epsilon}_{o,i})\cos\delta_i}\right)-\arctan\left(\frac{-\sum_{i=1}^{N}(I_{r,i}+\bar{\epsilon}_{r,i})\sin\delta_i}{\sum_{k=1}^{N}(I_{r,i}+\bar{\epsilon}_{r,i})\cos\delta_i}\right)\right)}, \quad (20)$$

$$z_{MC,l} = \frac{Pd}{2\pi L}\left(\arctan\left(\frac{-\sum_{i=1}^{N}(I_{o,i}+\bar{\epsilon}_{o,i})\sin\delta_i}{\sum_{i=1}^{N}(I_{o,i}+\bar{\epsilon}_{o,i})\cos\delta_i}\right)-\arctan\left(\frac{-\sum_{k=1}^{N}(I_{r,i}+\bar{\epsilon}_{r,i})\sin\delta_i}{\sum_{i=1}^{N}(I_{r,i}+\bar{\epsilon}_{r,i})\cos\delta_i}\right)\right). \quad (21)$$

We define pixel intensity noise $\bar{\epsilon}_{r,o}$ for the reference and the object images with jointly normal distributions [37–39], allowing arbitrary image-to-image correlation, i.e., $\bar{\epsilon}_{r,i} \sim N(\mu_{r,i}, \sigma_{r,i}, \Sigma_{r,ij})$ and $\bar{\epsilon}_{o,i} \sim N(\mu_{o,i}, \sigma_{o,i}, \Sigma_{o,ij})$, $i = 1...N$, where μ is the pixel intensity noise mean, σ is the pixel intensity noise standard deviation, and Σ is the image-to-image pixel intensity noise correlation. The j subscript allows for the cross correlation between noise statistics at different projection indexes. We also assume that the reference and object images could also be correlated with correlation matrix $\Sigma_{or,ij}$; in other words, this allows for the general possibility that the i-th projection object image noise could be correlated with the j-th projection reference image noise (in addition to the earlier allowance that individual reference and object images may be intra-correlated). In the MC simulations, a single measurement point was modeled with a height $z = 2.09$cm and the simulated DFP geometries L and d were selected as 5cm and 30cm, respectively, deliberately chosen to provide clear distinctions between the full model and linear model height distributions in Figure 2. Fringe pitch P was selected as 8.5mm and 4 projections were used. Table 1 shows the specific statistics of the pixel intensity noise used for model verification.

Figure 2 shows the agreement between the analytically derived height uncertainty for both full

Parameter	**Variable**	**Quantity (Figure 2A)**	**Quantity (Figure 2B)**
Reference image pixel noise std.	σ_r	$\{0.175, 0.22, 0.145, 0.05\}$	$\{0.175, 0.22, 0.145, 0.05\}$, $\{0.525, 0.66, 0.435, 0.465\}$
Object image pixel noise std.	σ_o	$\{0.54, 0.36, 0.45, 0.36\}$	$\{0.18, 0.12, 0.15, 0.12\}$, $\{0.54, 0.36, 0.45, 0.36\}$
Reference image pixel noise correlation matrices	ρ_r	$\begin{pmatrix} 1. & 0.203 & 0.143 & 0.1 \\ 0.203 & 1. & 0.043 & 0.302 \\ 0.143 & 0.043 & 1. & 0.078 \\ 0.1 & 0.302 & 0.078 & 1. \end{pmatrix}$, $\begin{pmatrix} 1. & 0.691 & 0.774 & 0.86 \\ 0.691 & 1. & 0.855 & 0.696 \\ 0.774 & 0.855 & 1. & 0.769 \\ 0.86 & 0.696 & 0.769 & 1. \end{pmatrix}$	$\begin{pmatrix} 1. & 0.601 & 0.493 & 0.594 \\ 0.601 & 1. & 0.54 & 0.4 \\ 0.493 & 0.54 & 1. & 0.768 \\ 0.594 & 0.4 & 0.768 & 1. \end{pmatrix}$
Object image pixel noise correlation matrices	ρ_o	$\begin{pmatrix} 1. & 0.297 & 0.25 & 0.099 \\ 0.297 & 1. & 0.401 & 0.202 \\ 0.25 & 0.401 & 1. & 0.292 \\ 0.099 & 0.202 & 0.292 & 1. \end{pmatrix}$, $\begin{pmatrix} 1. & 0.886 & 0.751 & 0.785 \\ 0.886 & 1. & 0.774 & 0.895 \\ 0.751 & 0.774 & 1. & 0.65 \\ 0.785 & 0.895 & 0.65 & 1. \end{pmatrix}$	$\begin{pmatrix} 1. & 0.597 & 0.501 & 0.599 \\ 0.597 & 1. & 0.401 & 0.5 \\ 0.501 & 0.401 & 1. & 0.503 \\ 0.599 & 0.5 & 0.503 & 1. \end{pmatrix}$

Table 1: Figure 2 Simulation Parameters

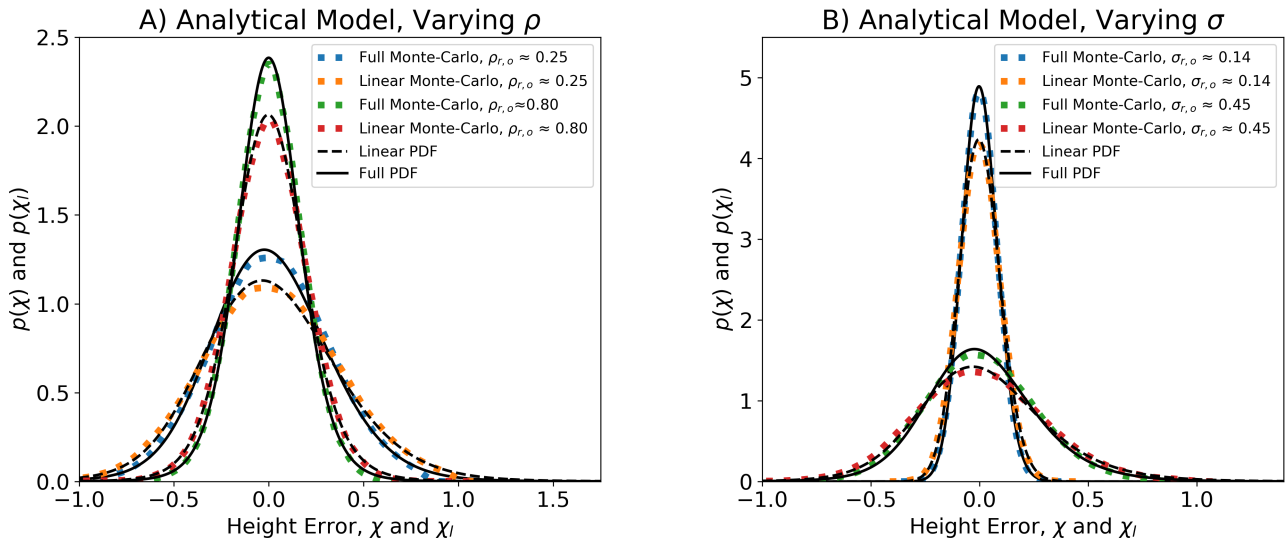

Figure 2: $p(\chi)$ and $p(\chi_l)$ from Equations 12 and 17 compared to Monte-Carlo simulations generated according to Equations 20 and 21. (A) shows two levels of pixel noise correlation. (B) shows two levels of pixel noise standard deviation.

and linear models and MC noise simulations. Excellent agreement is observed between the derived height uncertainty distributions and the MC simulations, across a variety of correlation cases and noise standard deviations.

3.2 Experimental Verification

3.2.1 Experiment Overview

To further assess the validity of our model, we compared the linearized height uncertainty model to experimental height measurement maps with a prototype DFP system. We evaluated our height uncertainty model under assumed ergodic conditions, i.e. that the distribution of phase values of many iterations of a measurement point would approach the inherent uncertainty of a single phase measurement point. A DFP experiment was conducted 85 times (referred onward as 85 iterations) using projections $N = 10, 14$, and 18, measuring an unmoved, identical surface for the object and reference plane. This experiment was conducted using the standard 8-bit imaging capabilities of the camera system, and then repeated using the "BaslerBG12" setting which captures three-channel color images in 12-bit depth projections $N = 10$,and 14, which were converted to mono-color 16-bit depth prior to image processing [40]. We chose to perform the experiment with camera capturing with two different bit depths to observe the effects of pixel value quantization on phase error relative to pixel intensity noise.

Using a single, unmoved surface ensured two factors; first, that the true height value z for each measurement pixel is known as 0, and second, that the distribution of height noise across all iterations on the height map provided by the DFP system was not caused by mismatched subtleties in the height of the measured object. The known height map of 0 allowed the usage of the linearized height uncertainty model from Equations 17 and 19 (special case). The 85 iterations recorded for each phase shifted projection, were used for statistical computation of the inputs for the model, ($\sigma_r, \sigma_o, \rho_r, \rho_o$, and ρ_{ro}). A height map was created from the phase map for each iteration using a calibration routine

Figure 3: 2 combined photographs of prototype DFP system. Illumination is shown by splicing a second image with shorter exposure to illustrate projected pattern.

described in [36, 41]; this resulted in the measured value of $L/(Pd)$ =1.54 mm/rad. The amount of iterations was chosen to provide a middle ground between ability to accurately estimate noise statistics, and ambient pixel intensity fluctuation between captures. A full field map of ϕ_c (describing the carrier phase, and incorporated in terms σ_Y, σ_X, and ρ_{XY}) was constructed from the unwrapped reference phase measurement ϕ_r. Using the unwrapped phase measurement to account for the carrier phase, as opposed to simply using pixel index, allowed adaptation to possible mismatched viewing angle of fringes (not perfectly horizontal or vertical). Finally, the distribution of all 85 height values at each pixel in the measured area were compared to the linearized derived height uncertainty model $p(\chi_l)$ to assess the accuracy of the derived model.

The measurement system was comprised of a Vivitek Qumi Q5 handheld projector with the stock lens removed and fitted with a sigma DLSR focusing lens, and a Basler ace acA4600-7gc color GigE camera equipped with 35mm fixed focal length lens. The modification of the projector lens allowed for focusing the projection onto a smaller, higher resolution area for height measurement. A side effect of using the custom projector lens was the addition of wavelength-based aberrations while using white light fringe projection. These aberrations were mitigated by projecting green single-color fringes. We were unable to synchronize the frames of the projector with the camera shutter which caused strong "draw lines" in each image. We opted to mitigate these artifacts by increasing the exposure time of the projector to approximately 500ms, tightening the camera aperture and using a neutral density filter to further reduce illumination. A gamma calibration routine similar to that detailed in [36] was used to correct the nonlinear gamma effects of the projection and ensure more-sinusoidal fringe projection. The experimental field of view was 460x460 pixels. We decided to use the large number of projections to further mitigate the aberrations caused by the "draw lines" of the projector. The distance between

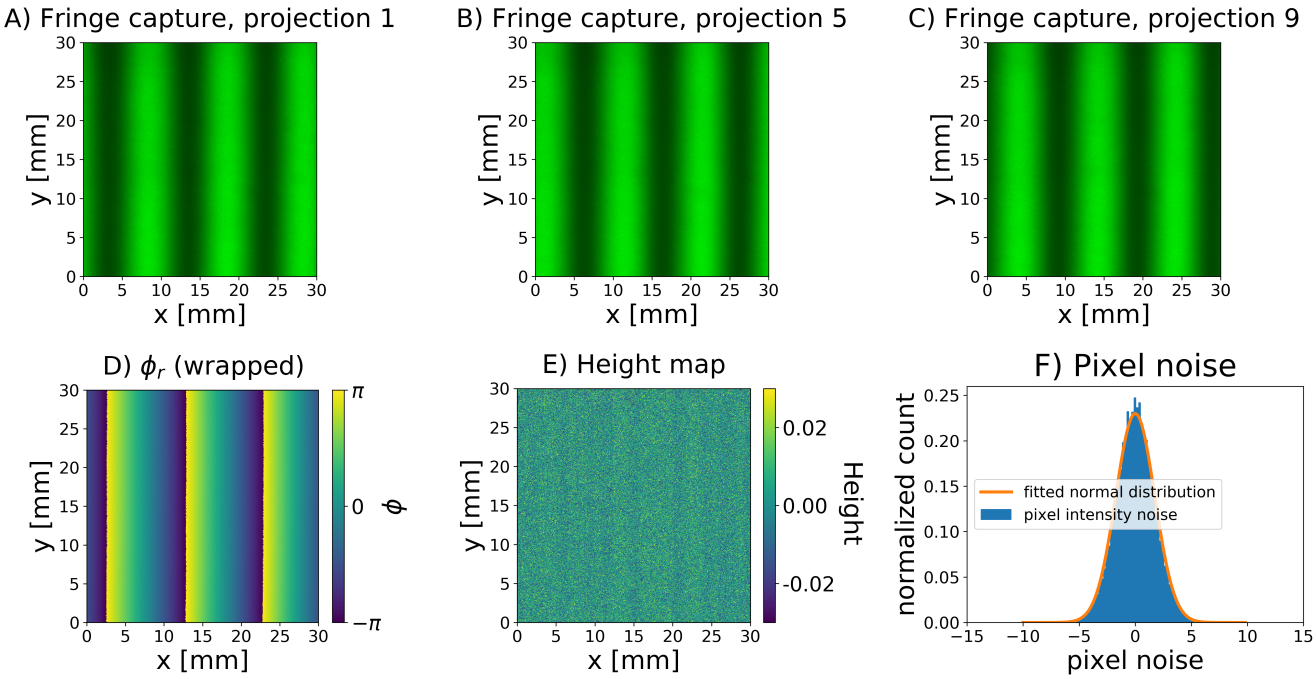

Figure 4: (A) through (C) shows the images captures of reference fringe projections. (D) shows the unwrapped reference phase map. (E) shows the height map of a single experiment iteration. (F) shows the distribution of pixel intensity noise with a fitted normal distribution.

the camera and projector L was approximately 230 [mm] and the distance between the projector and the measurement surface d was approximately 760 [mm]. The projected fringe pitch P was set to be 80 pixels, which corresponded to a physical pitch of approximately 12 [mm].

Figure 4 shows examples of the DFP height measurement process using images with 8-bit depth and 14 projections. We present the examples of the measurement process in the 8-bit depth range to provide results that may be more representative of common DFP setups. Figure 4A-C shows a sample of the captured incident fringes on the reference surface, each image having a unique phase shift δ_i. Figure 4D shows an example wrapped phase map of the reference surface, before the spatial unwrapping procedure is applied to remove 2π discontinuities. Figure 4E shows an example height map of a single measurement iteration. Figure 4F shows a sample distribution of raw pixel noise, with a fitted normal distribution, verifying our selection to model pixel intensity noise as a normally distributed random variable in our phase uncertainty derivation for $p(\kappa)$, and thus $p(\chi)$. In this figure, the pixel noise is shown with units of intensity not yet normalized by the fringe contrast. Pixel intensity units are by nature integers quantized by the camera, and here we show them as the difference to their mean, which is a decimal numerable, allowing for non-integer components in the histogram presented.

The images collected during the 85 iteration DFP height measurement procedure were used to determine the noise statistics which are the input to our uncertainty model. Figure 5 shows a collection of plots that illustrate the measured structure of pixel noise for the 14 projection DFP experiment. Figure 5A shows the pixel standard deviation, with the primary y-axis showing the pixel intensity standard deviation (before normalizing to the fringe contrast), and the secondary y-axis shows the pixel intensity standard deviation $\sigma_{r,o}$ normalized by fringe contrast, found by dividing the raw standard deviation by the measured fringe contrast for each pixel. We observed that the standard deviation was positively related to the pixel intensity which is significant due to its impact on the assumptions

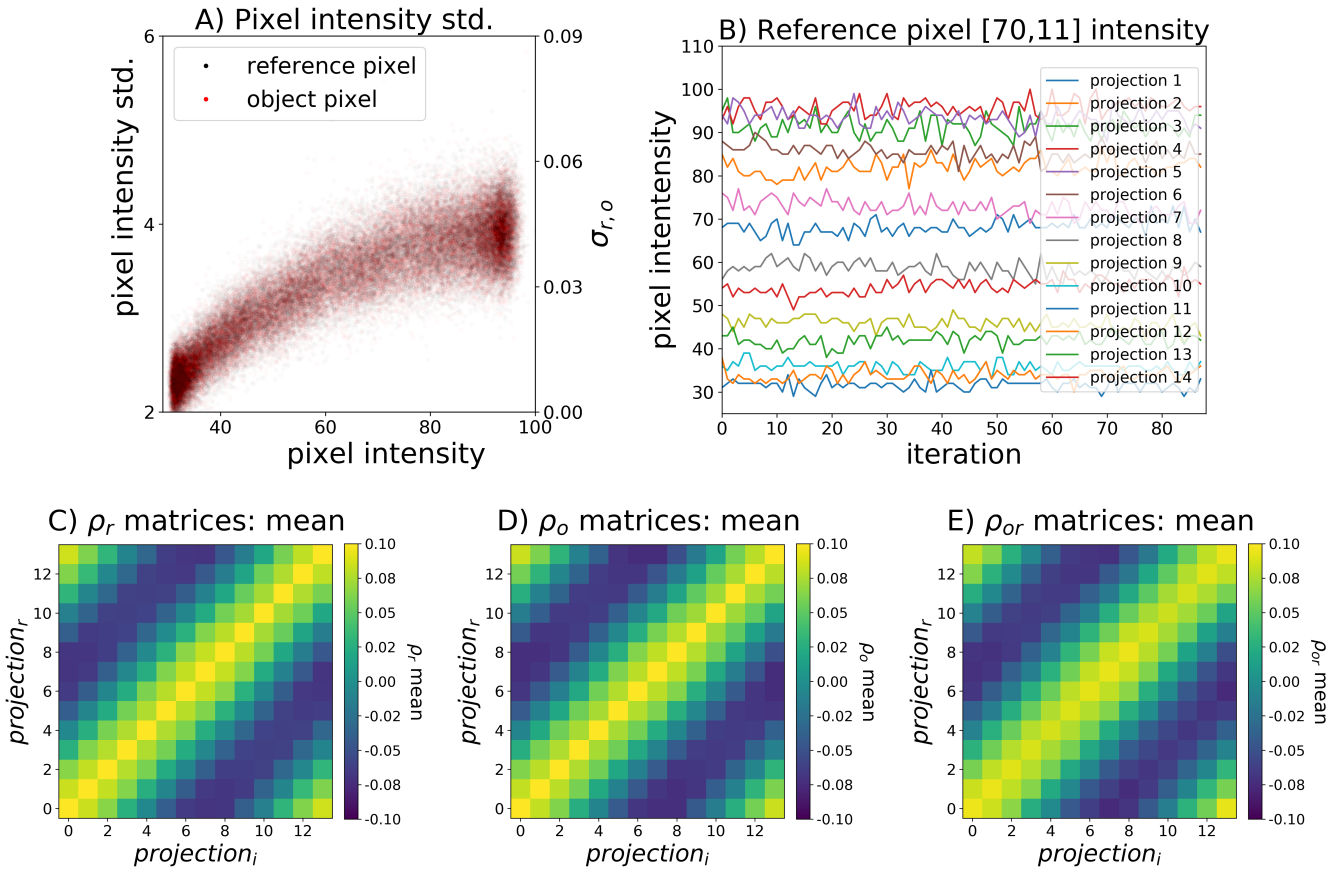

Figure 5: (A) shows the relationship between pixel intensity and pixel intensity noise. (B) shows the measured pixel intensity of a single pixel across all projections and all 85 iterations. (C) through (E) shows the mean correlation matrices across all pixels for the reference, object, and between reference and object, respectively.

required for the special case described in Section 2.1. Figure 5B shows a single pixel's intensity value across all 14 fringe projection projections, for each iteration, on the object image. For each pixel, $\rho_{r,ij}$ was estimated by finding the correlation of intensity values of projection "i" and projection "j" on the reference plane, and similarly for $\rho_{o,ij}$ on the object plane. For each pixel, $\rho_{ro,ij}$ was estimated by finding the correlation of intensity values of projection "i" on the reference plane, and projection "j" on the object plane. We observed that each off-diagonal term in ρ_o and ρ_r were approximately normally distributed, allowing for their means and standard deviations to accurately summarize their distributions. Figure 5C-E show the standard mean of ρ_r, ρ_o, and ρ_{ro} averaged across all pixels in the measurement scene, respectively. For this 8-bit, 14 projection experiment, we observed a trend of low, positive correlation of pixel intensity noise with nearest-to-diagonal terms approximately $0.07 - 0.08$. A slight structure can be observed in the off-diagonal terms of the correlation matrices; near-diagonal terms (representing images captured temporary close), as well as farthest-from-diagonal (outermost), exhibiting the highest correlation. The non-identity correlation structures measured in experiment are significant due to their impact on the assumptions required for the special case described in Section 2.1.

3.2.2 Experimental Results

Results comparing the experimental distribution of measured height values to the estimation of height uncertainty, $p(\chi_l)$, are shown in Figure 6 and a summary of the results in Table 2. Figures 6A-D shows results from the DFP experiment using 8-bit images, while Figures 6E-F show results using 12-bit images. Figure 6A shows a comparison of an example pixel's height distribution across all experiment iterations compared to $p(\chi_l)$ estimated using the pixel's image intensity statistics $\sigma_r, \sigma_o, \rho_r, \rho_o$, and ρ_{ro} measured from the experiment. In order to report the accuracy of our height uncertainty model for every pixel in the measured area, a performance metric $\bar{\lambda}$ was created that represents the normalized difference of the estimated height uncertainty and the distribution of height measurements across all iterations. Each pixel in $\bar{\lambda}$ is calculated using $\bar{\lambda} = (\sigma_m - \sigma_e)/\sigma_m$, where σ_m is the standard deviation of the measured heights of each pixel, and σ_e is the standard deviation of $p(\chi_l)$. The error map is constructed to provide positive values when $p(\chi_l)$ underestimates the standard deviation of the height distribution. Figure 6B shows the normalized difference map $\bar{\lambda}$ for every pixel in the measured area, using the linearized height uncertainty model $p(\chi_l)$ from Equation 17 and measured noise correlation statistics. Figure 6C shows the normalized difference map $\bar{\lambda}$ when using the simplified model from Equation 19 for the special case from Section 2.1, i.e. assuming no pixel noise correlation and using the average pixel noise standard deviation across all projections. The example measurement noise statistics provided in Figure 5 show that there was in fact noise correlation in our experiment, meaning that the special case assumptions of Equation 19 will induce error. This causes the normalized difference map $\bar{\lambda}$ in Figure 6C to differ from Figure 6B, shifting from positive to negative mean.

Figure 6D shows the distributions of normalized difference maps $\bar{\lambda}$ for the full and special cases, for all 3 8-bit experiments using $N = 10, 14, 18$ projections. We observed that our height error prediction performed better in cases with higher N, a reason for this trend may be that projector gamma error is reduced when using more projections [42]. The distributions of $\bar{\lambda}$ created from $p(\chi_l)$ using correlation statistics were positively biased by 2.2%, 1.9%, 3.7% and with standard deviations of 8.2%, 8.0%, and 7.8% for the experiments using 10, 14, and 18 projections, respectively. The distributions of $\bar{\lambda}$

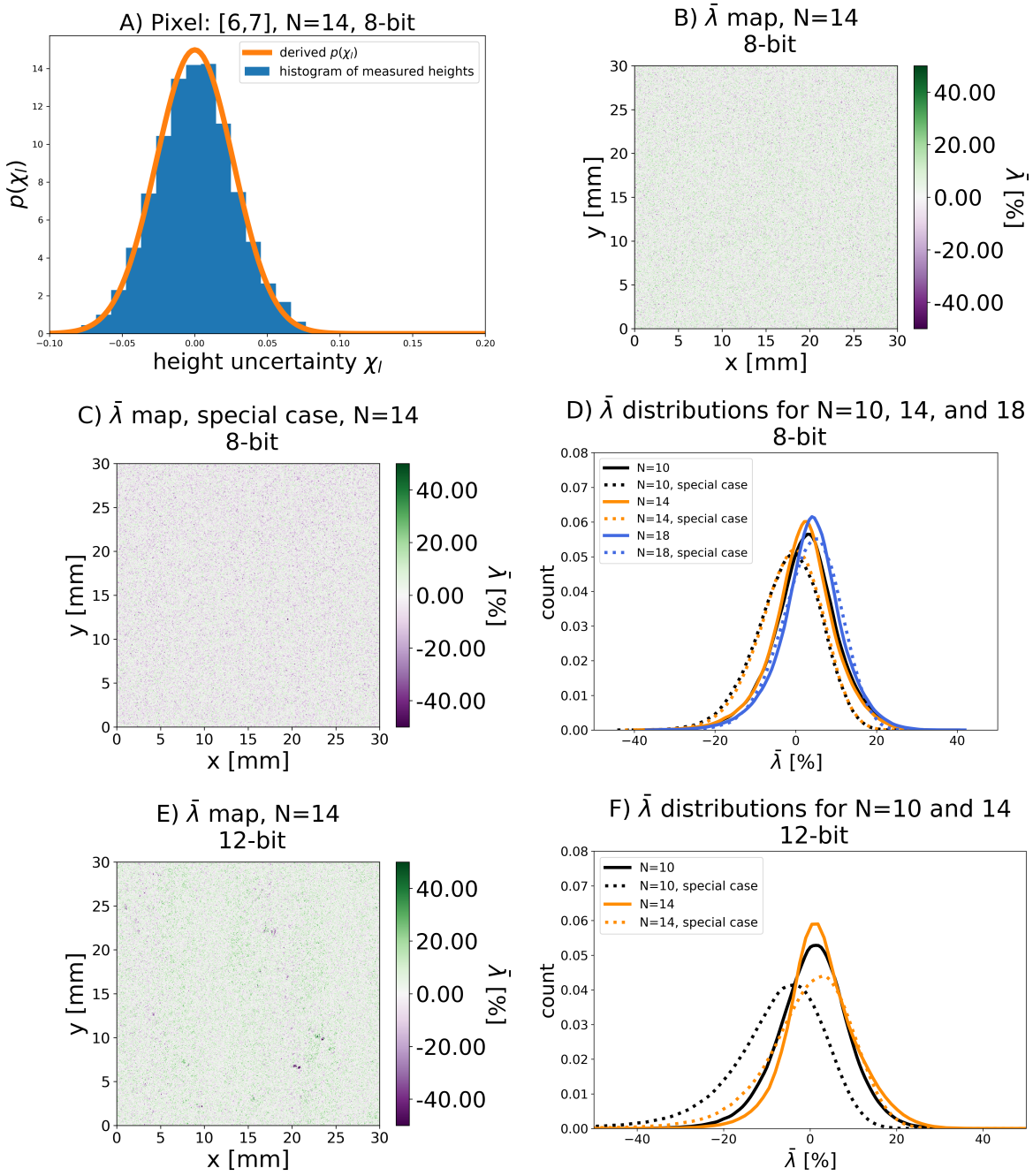

Figure 6: (A) shows a single pixel's experimental distribution of heights from all 85 measurements compared to its estimated height uncertainty $p(\chi_l)$ for the 8-bit image capture experiment. (B) shows the normalized difference map of all of the pixels in the measurement area using all of the available noise statistics for the 8-bit image capture experiment. (C) shows the normalized difference map of all of the pixels in the measurement area assuming that there is no pixel noise correlation and the standard deviation of the pixel noise is constant throughout all of the projections, for the 8-bit image capture experiment. (D) shows distributions of the error maps for $N = 10, 14$, and 18 projections in the 8-bit image capture experiment. (E) and (F) show the 14 projection normalized difference map and the distributions of error maps for $N = 10$ and 14, for the 12-bit image capture experiment.

			Bias	Standard deviation	Mean off-diagonal $\rho_{r,o,ro}$ value
8-bit	Full linear model	10 projections	+2.2%	8.2%	$\rho \approx 0.08 - 0.09$
		14 projections	+1.9%	8.0%	$\rho \approx 0.07 - 0.08$
		18 projections	+3.7%	7.8%	$\rho \approx 0.02 - 0.03$
	Special case	10 projections	-1.9%	10.5%	$\rho \approx 0.08 - 0.09$
		14 projections	-1.4%	8.6%	$\rho \approx 0.07 - 0.08$
		18 projections	+3.6%	7.4%	$\rho \approx 0.02 - 0.03$
12-bit	Full linear model	10 projections	+0.9%	9.3%	$\rho \approx 0.13 - 0.20$
		14 projections	+2.5%	8.1%	$\rho \approx 0.11 - 0.22$
	Special case	10 projections	-8.7%	14.5%	$\rho \approx 0.13 - 0.20$
		14 projections	-0.5%	10.7%	$\rho \approx 0.11 - 0.22$

Table 2: $\bar{\lambda}$ distribution statistics

created from $p(\chi_l)$ predicting a tighter height uncertainty than measured in experiment, which we hypothesize is due to other sources of error entering the height calculation such as external vibrations, subtle environmental lighting fluctuations, gamma error, and projector draw lines.

$\bar{\lambda}$ distributions created from ignoring noise correlation (special case) for 8-bit experiments using 10 and 14 projections were slightly negatively biased by -1.9% and -1.4%,with standard deviations of 10.5% and 8.6%, respectively. We hypothesize that this is because the introduction of correlation reduces height uncertainty, as shown in Figure 2A, and assuming no correlation exists increases the height uncertainty estimation made by our model. $\bar{\lambda}$ distributions from the 18 projection experiment created from ignoring noise correlation was positively biased by 3.6%, with a standard deviation of 7.4% and considerably closer to the full model's error distribution; we hypothesize that this is due to very low levels of correlation during the 18 projection experiment (averages of the near-diagonal terms of the ρ matrices were approximately 0.02 during the 18 projection experiment as opposed to 0.08 for both 10 and 14 projection experiments).

Figures 6E and F show the effects of using 12-bit imaging. We observed similar model height estimation error for these experiments compared to the 8-bit image capture experiments, suggesting that our uncertainty model's performance is independent of pixel quantization effects. A key difference in the experiment was that our observed pixel noise correlation was much higher when using 12-bit images (see Table 2). A formal analysis of the quantization occurring within the camera was considered, but deemed out of the scope of this paper. Figure 6E is positively biased, similar to its 8-bit counterpart in Figure 6B, and Figure 6F shows similar distributions to its 8-bit counterpart in Figure 6D. The

model estimation accuracy bias for 12-bit full cases for $N = 10$ and 14 are 0.9% and 2.5%, and standard deviations of 9.3% and 8.1%, respectively. For the special case, estimation biases were recorded as -8.7% and -0.5% and with standard deviations of 14.5% and 10.7%, for $N = 10$ and 14, respectively. We attribute the large negative bias for the 10 projection special case to be the large amount of correlation observed through the experiment (off-diagonal terms averaging around 0.15) We were unable to perform an 18 projection experiment using 12-bit imaging depths due to memory and hardware constraints.

4 Conclusions

A height-converted image intensity noise uncertainty model (Equation 12) was derived as a continuation of the phase-converted image intensity noise uncertainty model from [34]. As the DFP height profiling process is often linearized during practice, a linearized model (Equation 17) was also derived. Additionally, simplified versions of the full and linear height uncertainty models (Equations 14 and 19)were proposed according to special assumptions regarding pixel intensity noise statistics. The full and linearized height uncertainty models were verified against a variety of noise structures with varying levels of correlation and noise standard deviation. Excellent agreement was achieved between the model and simulations, shown in Figure 2. The height uncertainty model was also compared to an ensemble of 85 real DFP experiments each with 8-bit and 12-bit camera images, where an area of 30x30mm (460x460 pixels) was measured. Noise statistics were recorded and used as inputs for the height uncertainty model, and the distribution of height measurements was compared to the height uncertainty model for each pixel, shown in Figure 6. In general, our full statistical model was observed to predict the height measurement uncertainty with error below 11% for the 8-bit depth images, and below 9% for the 12-bit depth images. The effect of ignoring correlation increased our model error proportionally to the amount of correlation observed.

The significance of this research is to provide a probability density function model which estimates the height measurement uncertainty of the DFP technique using observable pixel intensity fluctuation statistics in the pixel field domain; from such a density function, any order statistics may be computed. Advancement of this model currently includes work involving (1) verifying this model against three-dimensional objects with known height profiles, (2) using this model to quantify existence of small surface features with non-zero height profiles, (3) establishing optimization in the DFP measurement process to determine which averaging methods, exposure settings, and projection number will minimize height uncertainty.

Acknowledgement

This research was funded by Los Alamos National Laboratory (LANL) through the Engineering Institute - a research and education collaboration between LANL and the University of California San Diego's Jacobs School of Engineering. This collaboration seeks to promote multidisciplinary engineering research that develops and integrates advanced predictive modeling, novel sensing systems, and new developments in information technology to address LANL mission-relevant problems. LA-UR-20-24755.

References

[1] C. J. Moore, D. R. Burton, O. Skydan, P. J. Sharrock, and M. Lalor, "3D body surface measurement and display in radiotherapy part I: Technology of structured light surface sensing," in International Conference on Medical Information Visualisation-BioMedical Visualisation (MedVis' 06), pp. 97–102, IEEE, 2006.

[2] F. Lilley, M. J. Lalor, and D. R. Burton, "Robust fringe analysis system for human body shape measurement," Optical Engineering, vol. 39, pp. 187–195, 2000.

[3] K. Genovese and C. Pappalettere, "Whole 3D shape reconstruction of vascular segments under pressure via fringe projection techniques," Optics and Lasers in Engineering, vol. 44, no. 12, pp. 1311–1323, 2006.

[4] P.-R. Jang, R. Arunkumar, T. Leone, Z. Long, M. A. Mott, O. P. Norton, W. P. Okhuysen, Y. Su, D. L. Monts, and P. G. Kirk, "Quantitative imaging characterization of aluminum pit corrosion in Oak Ridge research reactor pool," in Advanced Environmental, Chemical, and Biological Sensing Technologies IV, vol. 6377, p. 63770S, International Society for Optics and Photonics, 2006.

[5] P. S. Huang, F. Jin, and F.-P. Chiang, "Quantitative evaluation of corrosion by a digital fringe projection technique," Optics and Lasers in Engineering, vol. 31, no. 5, pp. 371–380, 1999.

[6] R. Ernst, A. Weckenmann, and R. Velgan, "Local wall thickness measurement of formed sheet metal using fringe projection technique," in XVII IMEKO World Congress, Metrology in the 3rd Millennium. Croatia, pp. 1802–1805, Citeseer, 2003.

[7] C. Quan, C. J. Tay, X. Y. He, X. Kang, and H. M. Shang, "Microscopic surface contouring by fringe projection method," Optics and Laser Technology, vol. 34, no. 7, pp. 547–552, 2002.

[8] X. Y. He, W. Sun, X. Zheng, and M. Nie, "Static and dynamic deformation measurements of micro beams by the technique of digital image correlation," in Key Engineering Materials, vol. 326, pp. 211–214, 2006.

[9] H. Guo, H. He, and M. Chen, "Gamma correction for digital fringe projection profilometry," Applied Optics, vol. 43, no. 14, pp. 2906–2914, 2004.

[10] S. Ma, C. Quan, R. Zhu, L. Chen, B. Li, and C. J. Tay, "A fast and accurate gamma correction based on Fourier spectrum analysis for digital fringe projection profilometry," Optics Communications, vol. 285, no. 5, pp. 533–538, 2012.

[11] T. Hoang, B. Pan, D. Nguyen, and Z. Wang, "Generic gamma correction for accuracy enhancement in fringe-projection profilometry," Optics Letters, vol. 35, no. 12, pp. 1992–1994, 2010.

[12] M. J. Baker, J. Xi, and J. F. Chicharo, "Elimination of non-linear luminance effects for digital video projection phase measuring profilometers," in 4th IEEE international symposium on electronic design, test and applications (delta 2008), pp. 496–501, IEEE, 2008.

[13] X.-Y. Su, W.-S. Zhou, G. Von Bally, and D. Vukicevic, "Automated phase-measuring profilometry using defocused projection of a Ronchi grating," Optics Communications, vol. 94, no. 6, pp. 561–573, 1992.

[14] S. Lei and S. Zhang, "Flexible 3-D shape measurement using projector defocusing," Optics letters, vol. 34, no. 20, pp. 3080–3082, 2009.

[15] Z. Lei, C. Wang, and C. Zhou, "Multi-frequency inverse-phase fringe projection profilometry for nonlinear phase error compensation," Optics and Lasers in Engineering, vol. 66, pp. 249–257, 2015.

[16] T. Maack and R. Kowarschik, "Camera influence on the phase-measurement accuracy of a phase-shifting speckle interferometer," Applied optics, vol. 35, no. 19, pp. 3514–3524, 1996.

[17] P. S. Huang, Q. J. Hu, and F.-P. Chiang, "Double three-step phase-shifting algorithm," Applied optics, vol. 41, no. 22, pp. 4503–4509, 2002.

[18] J. Pan, P. S. Huang, and F.-P. Chiang, "Color-coded binary fringe projection technique for 3-D shape measurement," Optical Engineering, vol. 44, no. 2, p. 23606, 2005.

[19] Y. C. Kai and K. S. Yen, "Compensation of gamma effect and color cross talk in color-coded fringe profilometry," Journal of Electronic Imaging, vol. 29, no. 2, p. 23021, 2020.

[20] C. Chen, N. Gao, X. Wang, Z. Zhang, F. Gao, and X. Jiang, "Generic exponential fringe model for alleviating phase error in phase measuring profilometry," Optics and Lasers in Engineering, vol. 110, pp. 179–185, 2018.

[21] A. Kamagara, X. Wang, and S. Li, "Nonlinear gamma correction via normed bicoherence minimization in optical fringe projection metrology," Optical Engineering, vol. 57, no. 3, p. 34107, 2018.

[22] G. Wu, Y. Wu, X. Hu, M. Wu, S. Zhang, and F. Liu, "Exponential Taylor Series Method to eliminate the gamma distortion in phase shifting profilometry," Optics Communications, vol. 452, pp. 306–312, 2019.

[23] J. Deng, H. Deng, J. Zhang, and L. Yu, "Studies of different error elimination algorithms under defocusing digital fringe projection," in Seventh International Symposium on Precision Mechanical Measurements, vol. 9903, p. 99032Q, International Society for Optics and Photonics, 2016.

[24] X. U. Zi-Xin and Y.-H. Chan, "Removing harmonic distortion of measurements of a defocusing three-step phase-shifting digital fringe projection system," Optics and Lasers in Engineering, vol. 90, pp. 139–145, 2017.

[25] Y. Li, J. Chen, Y. Tu, and H. Wang, "On bit-depth of pattern in three-dimensional measurement system based on digital fringe projection," in International Conference on Optical and Photonics Engineering (icOPEN 2016), vol. 10250, p. 1025018, International Society for Optics and Photonics, 2017.

[26] C. Zuo, S. Feng, L. Huang, T. Tao, W. Yin, and Q. Chen, "Phase shifting algorithms for fringe projection profilometry: A review," Optics and Lasers in Engineering, vol. 109, pp. 23–59, 2018.

[27] D. J. Bone, H.-A. Bachor, and R. J. Sandeman, "Fringe-pattern analysis using a 2-D Fourier transform," Applied Optics, vol. 25, no. 10, pp. 1653–1660, 1986.

[28] F. Becker and H. Y. Yung, "Digital fringe reduction techniques applied to the measurement of three-dimensional transonic flow fields," Optical Engineering, vol. 24, no. 3, p. 243429, 1985.

[29] G. H. Notni and G. Notni, "Digital fringe projection in 3D shape measurement: an error analysis," in Optical Measurement Systems for Industrial Inspection III, vol. 5144, pp. 372–380, International Society for Optics and Photonics, 2003.

[30] K. Creath, "Step height measurement using two-wavelength phase-shifting interferometry," Applied optics, vol. 26, no. 14, pp. 2810–2816, 1987.

[31] Y. An, Z. Liu, and S. Zhang, "Evaluation of pixel-wise geometric constraint-based phase-unwrapping method for low signal-to-noise-ratio (SNR) phase," Advanced Optical Technologies, vol. 5, no. 5-6, pp. 423–432, 2016.

[32] Y. An, J.-S. Hyun, and S. Zhang, "Pixel-wise absolute phase unwrapping using geometric constraints of structured light system," Optics express, vol. 24, no. 16, pp. 18445–18459, 2016.

[33] S. Tang and Y. Y. Hung, "Fast profilometer for the automatic measurement of 3-D object shapes," Applied Optics, vol. 29, no. 20, pp. 3012–3018, 1990.

[34] N. M. O'Dowd, A. J. Wachtor, and M. D. Todd, "A model for describing phase-converted image intensity noise in digital fringe projection techniques," Optics and Lasers in Engineering, vol. 134, p. 106293, 2020.

[35] M. Halioua and H.-C. Liu, "Optical three-dimensional sensing by phase measuring profilometry," Optics and Lasers in Engineering, vol. 11, no. 3, pp. 185–215, 1989.

[36] S. Zhang, High-Speed 3D Imaging with Digital Fringe Projection Techniques. CRC Press, USA, 2016.

[37] A. K. Jain, Fundamentals of Digital Image Processing. Englewood Cliffs, NJ: Prentice Hall,, 1989.

[38] J. Takamatsu, Y. Matsushita, and K. Ikeuchi, "Estimating camera response functions using probabilistic intensity similarity," in 2008 IEEE Conference on Computer Vision and Pattern Recognition, pp. 1–8, IEEE, 2008.

[39] B. Pan, K. Li, and W. Tong, "Fast, robust and accurate digital image correlation calculation without redundant computations," Experimental Mechanics, vol. 53, no. 7, pp. 1277–1289, 2013.

[40] Basler Corporation, "Basler Product Documentation: Pixel Format," 2020.

[41] N. M. O'Dowd and M. D. Todd, "Out-of-Plane Surface Measurement and Porosity Quantification Using Fringe Projection Structured Light System for use in Powder Bed Manufacturing," in Metal Additive Manufacturing Conference, pp. 229–238, 2019.

[42] B. Pan, Q. Kemao, L. Huang, and A. Asundi, "Phase error analysis and compensation for nonsinusoidal waveforms in phase-shifting digital fringe projection profilometry," Optics Letters, vol. 34, no. 4, pp. 416–418, 2009.